# CHAPTER 12

# INDUCTIVE DISCHARGES

The limitations of capacitive rf discharges and their magnetically enhanced variants have led to the development of various low-pressure, high-density plasma discharges. The distinction between low- and high-density discharges is described in Sections 10.1 and 10.2. A few examples are shown schematically in Figure 1.14, and typical parameters are given in Table 1.1. In addition to high density and low pressure, a common feature is that the rf or microwave power is coupled to the plasma across a dielectric window or wall, rather than by direct connection to an electrode in the plasma, as for a capacitive discharge. This noncapacitive power transfer is the key to achieving low voltages across all plasma sheaths at electrode and wall surfaces. The dc plasma potential, and hence the ion acceleration energy, is then typically 20–40 V at all surfaces. To control the ion energy, the electrode on which the substrate is placed can be independently driven by a capacitively coupled rf source. Hence independent control of the ion/radical fluxes (through the source power) and the ion-bombarding energy (through the substrate electrode power) is possible. The relation between substrate electrode power and ion-bombarding energy at the substrate is described in Chapter 11. High-density inductive rf discharges are described in this chapter, and high-density wave heated discharges are described in Chapter 13. Nonresonant inductive discharges operated at high densities and low pressures, which are driven at frequencies below the self-resonant frequency of the exciting coil, are described in Section 12.1. Other operating regimes and power transfer considerations are described in Section 12.2. The planar coil configuration, which is commonly used for materials processing, is described in Section 12.3, with emphasis on

*Principles of Plasma Discharges and Materials Processing*, by M. A. Lieberman and A. J. Lichtenberg.
ISBN 0-471-72001-1 

experimental measurements. Excitation at the self-resonant frequency leads to the *helical resonator* configuration, described in Section 12.4. Some other aspects of high-density discharges, including issues of plasma transport and substrate damage, are described in a review article by Lieberman and Gottscho (1994), from which some of the material in Chapters 12 and 13 is drawn.

## 12.1 HIGH-DENSITY, LOW-PRESSURE DISCHARGES

Inductive discharges are nearly as old as the invention of electric power, with the first report of an "electrodeless ring discharge" by Hittorf in 1884. He wrapped a coil around an evacuated tube and observed a discharge when the coil was excited with a Leyden jar. A subsequent 50-year controversy developed as to whether these discharges were capacitively driven by plasma coupling to the low- and high-voltage ends of the cylindrical coil, as in a capacitive discharge (see Chapter 11), or were driven by the induced electric field inside the coil. This issue was resolved with the recognition that the discharge was capacitively driven at low plasma densities, with a transition to an inductive mode of operation at high densities. Succeeding developments, which focused on pressures exceeding 20 mTorr in a cylindrical coil geometry, are described in a review article by Eckert (1986). The high-pressure regime was intensively developed in the 1970s with the invention of the open air induction torch and its use for spectroscopy. In the late 1980s, the planar coil configuration was developed, renewing interest in the use of high-density inductive discharges for materials processing at low pressures ($<$50 mTorr) and in low aspect ratio geometries ($l/R \lesssim 1$ for a cylindrical discharge). Such discharges can be driven with either planar or cylindrical coils. It is this regime that is the primary focus here.

Plasma in an inductive discharge is created by application of rf power to a nonresonant inductive coil. Inductive sources have potential advantages over high-density wave-heated sources, including simplicity of concept, no requirement for dc magnetic fields (as required for ECRs and helicons, discussed in Chapter 13), and rf rather than microwave source power. The nonresonant operation may be either an advantage or a disadvantage, depending on use; a resonant version, the *helical resonator*, is considered in Section 12.4.

In contrast to ECRs and helicons, which can be configured to achieve densities $n_0 \gtrsim 10^{13}$ cm$^{-3}$, as we will see in Chapter 13, inductive discharges may have natural density limits, $n_0 \lesssim 10^{13}$ cm$^{-3}$, for efficient power transfer to the plasma. However, the density regime $10^{11} \lesssim n_0 \lesssim 10^{12}$ cm$^{-3}$ for efficient inductive discharge operation, typically a factor of 10 times higher than for capacitive discharges, is of considerable interest for low-pressure processing. Inductive discharges for materials processing are sometimes referred to as TCPs (transformer-coupled plasmas), ICPs (inductively coupled plasmas), or RFI plasmas (rf inductive plasmas).

### Inductive Source Configurations

The two coil configurations, cylindrical and planar, are shown in Figure 12.1 for a low aspect ratio discharge. The planar coil is a flat helix wound from near the axis to

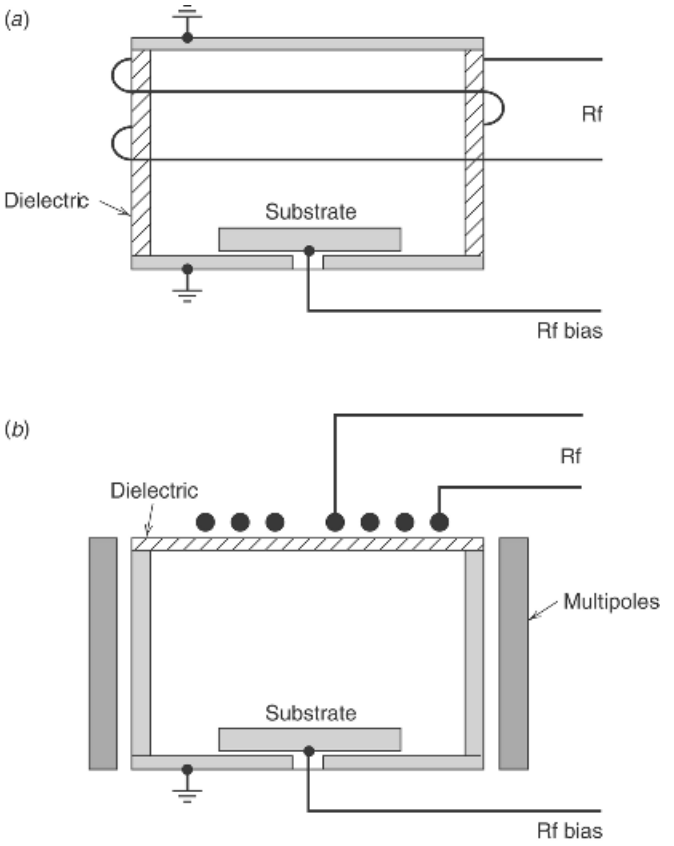


**Figure 12.1.** Schematic of inductively driven sources in (*a*) cylindrical and (*b*) planar geometries.

near the outer radius of the discharge chamber ("electric stove-top" coil shape). Multipole permanent magnets (see Section 5.6) can be used around the process chamber circumference, as shown in Figure 12.1*b*, to increase radial plasma uniformity. The planar coil can also be moved close to the wafer surface, resulting in a close-coupled or near-planar source geometry ($l < R$) having good uniformity properties even in the absence of multipole confinement. In the close-coupled configuration, the coil can be wound nonuniformly to control the radial plasma uniformity.

Inductive coils are commonly driven at 13.56 MHz or below, using a 50-Ω rf supply through a capacitive matching network, which we describe later in this section. The coil can also be driven push–pull using a balanced transformer, which places a virtual ground in the middle of the coil and reduces the maximum coil-to-plasma voltage by a factor of 2. This reduces the undesired capacitively coupled rf current flowing from coil to plasma by a factor of 2. An electrostatic shield placed between the coil and the plasma further reduces the capacitive

coupling if desired, while allowing the inductive field to couple unhindered to the plasma. For the dc plasma potential to be clamped to a low value, 20–40 V, in the presence of stray capacitive coupling from the exciting coil and from the capacitively driven substrate holder, it is essential that the plasma be in contact with a grounded metal surface of substantial area (see Fig. 12.1 and Section 11.4).

## Power Absorption and Operating Regimes

In an inductively coupled plasma, power is transferred from the electric fields to the plasma electrons within a skin depth layer of thickness $\delta$ near the plasma surface by collisional (ohmic) dissipation and by a collisionless heating process in which bulk plasma electrons "collide" with the oscillating inductive electric fields within the layer. In the latter situation, electrons are accelerated and subsequently thermalized much like stochastic heating in capacitive rf sheaths, which we discussed in Section 11.1. We first consider the ohmic heating process.

The spatial decay constant $\alpha$ within a plasma for an electromagnetic wave normally incident on the boundary of a uniform density plasma can be calculated as discussed in Section 4.2, and is (Problem 12.1)

$$\alpha = -\frac{\omega}{c}\text{Im } \kappa_p^{1/2} \equiv \delta^{-1} \tag{12.1.1}$$

From (4.2.18), the relative plasma dielectric constant is

$$\kappa_p = 1 - \frac{\omega_{pe}^2}{\omega(\omega - j\nu_m)} \approx -\frac{\omega_{pe}^2}{\omega^2(1 - j\nu_m/\omega)} \tag{12.1.2}$$

with $\omega_{pe}$ the plasma frequency near the boundary, and $\nu_m$ the electron–neutral momentum transfer frequency. There are two collisionality regimes.

(a) For $\nu_m \ll \omega$, we drop $\nu_m/\omega$ in (12.1.2) to obtain

$$\alpha = \frac{\omega_{pe}}{c} \equiv \frac{1}{\delta_p} \tag{12.1.3}$$

where $\delta_p$ is the collisionless skin depth. Substituting for $\omega_{pe}$ in (12.1.3), we find

$$\delta_p = \left(\frac{m}{e^2\mu_0 n_s}\right)^{1/2} \tag{12.1.4}$$

(b) For $\nu_m \gg \omega$, we drop the 1 in the parentheses of (12.1.2), expanding for $\nu_m \gg \omega$, and substituting the imaginary part of $\kappa_p^{1/2}$ into (12.1.1), we obtain

$$\alpha = \frac{1}{\sqrt{2}}\frac{\omega_{pe}}{c}\left(\frac{\omega}{\nu_m}\right)^{1/2} \equiv \frac{1}{\delta_c} \tag{12.1.5}$$

where $\delta_c$ is the collisional skin depth. Substituting for the dc conductivity $\sigma_{dc} = e^2 n_s / m\nu_m$ from (4.2.22), $\delta_c$ can be written in the forms

$$\delta_c = \delta_p \left(\frac{2\nu_m}{\omega}\right)^{1/2} = \left(\frac{2}{\omega\mu_0\sigma_{dc}}\right)^{1/2} \tag{12.1.6}$$

(c) There is a third situation (Weibel, 1967; Turner, 1993) for which electrons incident on a skin layer of thickness $\delta_e$ satisfy the condition

$$\frac{\bar{v}_e}{2\delta_e} \gg \omega, \nu_m \tag{12.1.7}$$

where $\delta_e$ is determined below. In this case, the interaction time of the electrons with the skin layer is short compared to the rf period or the collision time. In analogy to collisionless heating at a capacitive sheath, a stochastic collision frequency (18.5.2) can be defined

$$\nu_{stoc} = \frac{C_e \bar{v}_e}{4\delta_e} \tag{12.1.8}$$

where $C_e$ is a quantity of order unity that depends weakly on $\bar{v}_e, \delta_e$, and $\omega$, provided the ordering (12.1.7) is satisfied (see Section 18.5). We then substitute $\nu_{stoc}$ for $\nu_m$ in (12.1.2) and expand for $\nu_{stoc} \gg \omega$ as in (b), to obtain

$$\delta_e = \frac{c}{\omega_{pe}} \left(\frac{C_e \bar{v}_e}{2\omega\delta_e}\right)^{1/2}$$

Solving for $\delta_e$, we find

$$\delta_e = \left(\frac{C_e c^2 \bar{v}_e}{2\omega\omega_{pe}^2}\right)^{1/3} = \left(\frac{C_e \bar{v}_e}{2\omega\delta_p}\right)^{1/3} \delta_p \tag{12.1.9}$$

where $\delta_e$ is the *anomalous skin depth* (see Alexandrov et al., 1984).

At 13.56 MHz in argon, we find $\nu_m = \omega$ for $p^* \approx 25$ mTorr. We are interested primarily in the low-pressure regimes with $p \ll p^*$, which we consider first. For each pressure regime, we also distinguish two density regimes:

(a) High density, $\delta \ll R, l$
(b) Low density, $\delta \gtrsim R, l$

For typical low-pressure processing discharges, we are generally in the regime for which the frequency ordering is $\omega \sim \bar{v}_e / 2\delta \gtrsim \nu_m$ and such that the skin depth is approximately $\delta_p$. For typical plasma dimensions $R, l \sim 10$ cm, we are in the high

density regime. We shall discuss the high-pressure ($\nu_m \gg \omega$) and low-density ($\delta \gg R, l$) regimes later when we consider the minimum current and power necessary to generate an ICP.

### Discharge Operation and Coupling

Although many systems are operated with planar coils (see Fig. 12.1*b*), finite geometry effects make these configurations difficult to analyze. To illustrate the general principles of inductive source operation, we examine a uniform density cylindrical discharge (Fig. 12.1*a*) in the geometry $l \gtrsim R$. We take the coil to have $\mathcal{N}$ turns at radius $b > R$. Integrating the power flow into the plasma, with $\delta_p \ll R$, we have (Problem 12.2)

$$P_{abs} = \frac{1}{2}\frac{J_\theta^2}{\sigma_{eff}}\pi R l \delta_p \tag{12.1.10}$$

where $J_\theta$ is the amplitude of the induced rf azimuthal current density at the plasma edge near $r = R$ (opposite in direction to the applied azimuthal current in the coil). In analogy to the conductivity in (4.2.22),

$$\sigma_{eff} = \frac{e^2 n_s}{m\nu_{eff}} \tag{12.1.11}$$

with $\nu_{eff} = \nu_m + \nu_{stoc}$ as in (18.5.15), a sum of collisional and stochastic heating. An estimate for $\nu_{stoc}$ is given in (18.5.14) or Figure 18.5. Equation (12.1.10) is equivalently half the power loss of a uniform sinusoidal current density flowing within a skin thickness $\delta_p$. Letting $I_p = J_\theta l \delta_p$ be the total induced rf current amplitude in the plasma skin and defining the plasma resistance through $P_{abs} = \frac{1}{2} I_p^2 R_p$, we obtain

$$R_p = \frac{\pi R}{\sigma_{eff} l \delta_p} \tag{12.1.12}$$

As in (11.1.3) (see also Fig. 11.4), there is also a plasma inductance $L_p$, which accounts for the phase lag between the rf electric field and the rf conduction current due to the finite electron inertia. To determine this inductance, we integrate the electric field $E_\theta$ around the plasma loop to obtain the voltage $V = 2\pi R E_\theta$. Substituting $J_\theta$ in terms of $I_p$ and $E_\theta$ in terms of $V$ into ohm's law $J_\theta = \sigma_p E_\theta$, with $\sigma_p$ given by (4.2.20) (with $\nu_{eff}$ in place of $\nu_m$), we obtain the voltage-current relation $V = I_p(R_p + j\omega L_p)$, with $R_p$ given by (12.1.12) and with

$$L_p = \frac{R_p}{\nu_{eff}} \tag{12.1.13}$$

In addition to $L_p$, there is the usual magnetic energy storage inductance $L_{22}$, because the rf plasma current creates a magnetic flux $\Phi_p = L_{22} I_p$ linked by the

current. Using $\Phi_p = \mu_0 \pi R^2 H_z$, where $H_z = J_\theta \delta_p$ is the magnetic field produced by the skin current, we obtain

$$L_{22} = \frac{\mu_0 \pi R^2}{l} \tag{12.1.14}$$

Letting the coil have $\mathcal{N}$ turns at a radius $b \gtrsim R$, where $b - R$ is the "thickness" of the dielectric interface separating coil and plasma, then we can model the source as the transformer shown in Figure 12.2. Evaluating the inductance matrix for this transformer, defined through (Schwarz and Oldham, 1984)

$$\tilde{V}_{rf} = j\omega L_{11}\tilde{I}_{rf} + j\omega L_{12}\tilde{I}_p \tag{12.1.15}$$

$$\tilde{V}_p = j\omega L_{21}\tilde{I}_{rf} + j\omega L_{22}\tilde{I}_p \tag{12.1.16}$$

where the tildes denote the complex amplitudes, for example, $V_{rf}(t) = \text{Re}\,\tilde{V}_{rf}\,e^{j\omega t}$, we obtain (Problem 12.3)

$$L_{11} = \frac{\mu_0 \pi b^2 \mathcal{N}^2}{l} \tag{12.1.17}$$

$$L_{12} = L_{21} = \frac{\mu_0 \pi R^2 \mathcal{N}}{l} \tag{12.1.18}$$

Using $\tilde{V}_p = -\tilde{I}_p(R_p + j\omega L_p)$ (see Fig. 12.2) in (12.1.16) and inserting into (12.1.15), we can solve for the impedance seen at the coil terminals:

$$Z_s = \frac{\tilde{V}_{rf}}{\tilde{I}_{rf}} = j\omega L_{11} + \frac{\omega^2 L_{12}^2}{R_p + j\omega(L_{22} + L_p)} \tag{12.1.19}$$

We will assume the usual high density ordering $\delta_p \sim \delta_c \ll R$ for the validity of (12.1.12)–(12.1.14). With this ordering, it can easily be seen from (12.1.12)–(12.1.14) that $R_p^2 + \omega^2 L_p^2 \ll \omega^2 L_{22}^2$. Hence expanding the denominator in

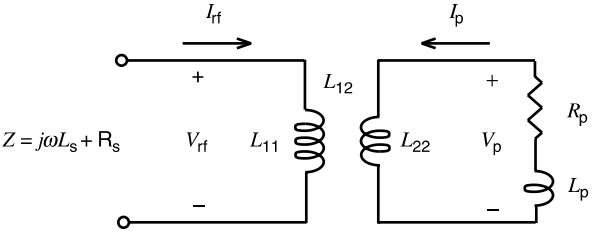


**Figure 12.2.** Equivalent transformer coupled circuit model of an inductive discharge.

(12.1.19), we obtain

$$L_s \approx \frac{\mu_0 \pi R^2 \mathcal{N}^2}{l}\left(\frac{b^2}{R^2} - 1\right) \tag{12.1.20}$$

$$R_s \approx \mathcal{N}^2 \frac{\pi R}{\sigma_{eff} l \delta_p} \tag{12.1.21}$$

where $Z_s = R_s + j\omega L_s$. The power balance,

$$P_{abs} = \frac{1}{2}|\tilde{I}_{rf}|^2 R_s \tag{12.1.22}$$

then yields the required rf source current, and the rf voltage is determined from

$$\tilde{V}_{rf} = \tilde{I}_{rf}|Z_s| \tag{12.1.23}$$

*Example* We let $R = 10$ cm, $b = 15$ cm, $l = 20$ cm, $\mathcal{N} = 3$ turns, $n_g = 1.7 \times 10^{14}$ cm$^{-3}$ (5 mTorr argon at 298 K), $\omega = 8.5 \times 10^7$ s$^{-1}$ (13.56 MHz), and $P_{abs} = 600$ W. At 5 mTorr, $\lambda_i \approx 0.6$ cm. Then from (10.2.1) and (10.2.2) $h_l \approx 0.20$, $h_R \approx 0.18$, and from (10.2.13), $d_{eff} \approx 18.2$ cm. For argon we then obtain from Figure 10.1 that $T_e \approx 2.8$ V, and from Figure 3.17, that $\mathcal{E}_c \approx 68$ V. From (10.2.4) we obtain $\mathcal{E}_i + 2T_e \approx 20$ V, and using (10.2.9), we find $\mathcal{E}_T \approx 88$ V. The Bohm velocity is $u_B \approx 2.6 \times 10^5$ cm/s, and from (10.2.11), $A_{eff} \approx 340$ cm$^2$. Then from (10.2.15), we obtain $n_0 \approx 4.8 \times 10^{11}$ cm$^{-3}$ and $n_s = h_R n_0 \approx 9.3 \times 10^{10}$ cm$^{-3}$. Estimating $\nu_m$ for argon from Figure 3.16, we find $\nu_m \approx 1.2 \times 10^7$ s$^{-1}$. Using (12.1.4), we find $\delta_p \approx 1.7$ cm. Evaluating $\nu_{stoc}$, we first find $\alpha \approx 2.2$ from (18.5.7). Then with $\bar{v}_e \approx 1.1 \times 10^8$ cm/s and $\delta = \delta_p$, we obtain $\nu_{stoc} \approx 2.8 \times 10^7$ s$^{-1}$ from Figure 18.5 or (18.5.14), such that $\nu_{eff} \approx 4.0 \times 10^7$ s$^{-1}$. Using this in (12.1.11), we find $\sigma_{eff} \approx 66$ mho/m. Evaluating (12.1.21) and (12.1.20), we find $R_s \approx 25\ \Omega$ and $L_s \approx 2.2\ \mu$H, such that $\omega L_s \approx 190\ \Omega$. Equations (12.1.22) and (12.1.23) then yield $I_{rf} \approx 9.9$ A and $V_{rf} \approx 1870$ V.

We note that $\omega > \nu_{eff}$ for this example, such that $\delta \approx \delta_p$, the collisionless skin depth, verifying our assumed ordering. We also note that stochastic heating somewhat dominates at this pressure: $\nu_{stoc} \sim 2\nu_m$. Godyak et al. (1993) have measured $\nu_{eff}$ in an inductive discharge, finding that $\nu_{eff}$ is independent of pressure at low pressures, indicating the dominance of stochastic over collisional heating. The measured $\nu_{eff}$ was $\sim 2\bar{v}_e/\delta_e$. For this experiment, $\delta_e \sim \delta_p \sim \delta_c$, so the scale length dependence could not be distinguished.

Because stochastically heated electrons are "kicked" in the skin layer and flow back into the bulk plasma with a characteristic thermal speed $v_{th}$, which is generally small compared to the phase velocity $v_{ph}$ of the wave, the electron current (carried by $v_{th}$) can become out-of-phase with the electric field (carried by $v_{ph}$) downstream from the skin layer, giving rise to regions of negative $\tilde{\mathbf{J}} \cdot \tilde{\mathbf{E}}$. For a phase change an odd multiple of $\pi$, $\omega t - kz = (2i - 1)\pi$, we would expect a series of

negative $\tilde{\mathbf{J}} \cdot \tilde{\mathbf{E}}$ regions centered about positions

$$z_i = \frac{\pi(2i-1)}{\dfrac{\omega}{v_{\text{th}}} - \dfrac{\omega}{v_{\text{ph}}}}, \qquad i = 1,2,\ldots$$

as has been observed experimentally (Godyak and Kolobov, 1997).

The rf magnetic field scales as $\tilde{\mathbf{B}} \sim \tilde{\mathbf{E}}/\omega\delta$ from (2.2.1), and the rf electron velocity scales as $\tilde{\mathbf{u}}_e \sim e\tilde{\mathbf{E}}/m\omega$ from (2.3.9). At low frequencies, $\tilde{\mathbf{B}}$ and $\tilde{\mathbf{u}}_e$ become large, leading to significant nonlinear inertial and Lorentz forces ($\tilde{\mathbf{u}}_e \cdot \nabla\tilde{\mathbf{u}}_e$ and $\tilde{\mathbf{u}}_e \times \tilde{\mathbf{B}}$ terms in (2.3.9)). These give rise to second harmonic ($2\omega$) rf currents and to ponderomotive forces (Smolyakov et al., 2003); the latter can expel low-energy electrons from the skin layer.

Under some conditions, the electron drift velocity associated with the induced rf plasma current within the skin depth layer can be larger than the electron thermal velocity. This drifting Maxwellian distribution with large mean energy can produce an increased ionization, leading to a lowering of $T_e$ and significant changes in the density profile over that found for the global (constant $T_e$) ionization model (10.2.12) (see Problem 12.4(b)).

### Matching Network

The high inductive voltage required for a three-turn coil can be supplied from a 50-Ω rf power source through a capacitive matching network, as shown in Figure 12.3. The admittance looking to the right at the terminals A–A′ is

$$Y_A \equiv G_A + jB_A = \frac{1}{R_s + j(X_1 + X_s)} \tag{12.1.24}$$

where the conductance is

$$G_A = \frac{R_s}{R_s^2 + (X_1 + X_s)^2} \tag{12.1.25}$$

and the susceptance is

$$B_A = -\frac{X_1 + X_s}{R_s^2 + (X_1 + X_s)^2} \tag{12.1.26}$$

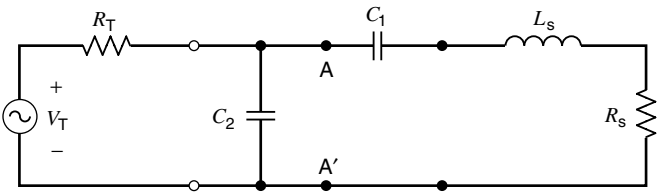


**Figure 12.3.** Equivalent circuit for matching an inductive discharge to a power source.

and where $X_1 = -(\omega C_1)^{-1}$. As described in Section 11.8, we must choose $G_A$ to be equal to $1/R_T$, for maximum power transfer, where $R_T = 50\ \Omega$ is the Thevenin-equivalent source resistance. For $R_s \approx 12.3\ \Omega$ and $X_s \approx 190\ \Omega$, we obtain from (12.1.25) that $X_1 \approx -168\ \Omega$. Hence $C_1 \approx 70$ pF. Evaluating $B_A$ for this value of $X_1$, we obtain $B_A \approx -0.035\ \Omega^{-1}$. We must choose $C_2$ to cancel this susceptance, that is, $B_2 = \omega C_2 = -B_A$, which determines $C_2 = 410$ pF to achieve the matched condition. In practice, $C_1$ and $C_2$ are variable capacitors that are tuned to achieve the match. The power absorption, $P_{abs} = \frac{1}{2} I_T^2 R_T$, then determines $I_T \approx 4.9$ A and $V_T = 2 I_T R_T \approx 490$ V.

## 12.2 OTHER OPERATING REGIMES

### Low-Density Operation

Since the effective conductivity $\sigma_{eff} \propto n_0$ and $\delta_p \propto n_0^{-1/2}$, it follows from (12.1.21) and (12.1.22) that at high densities:

$$P_{abs} \propto n_0^{-1/2} I_{rf}^2 \tag{12.2.1}$$

Hence at fixed $I_{rf}$, we have that $P_{abs} \propto n_0^{-1/2}$. However, at low densities, such that $\delta_p \gg R$, the conductivity is low and the fields fully penetrate the plasma. In this case expressions (12.1.12)–(12.1.14) are no longer correct. To find the absorbed power for this case, we apply Faraday's law to determine the induced electric field $E_\theta$ within the coil

$$E_\theta(r) = \frac{\frac{1}{2} j\omega r \mu_0 \mathcal{N} I_{rf}}{l} \tag{12.2.2}$$

and, writing $J_\theta = j\omega\epsilon_0\kappa_p E_\theta$ for $\nu_m \ll \omega$, we have $J_\theta \propto n_0 r I_{rf}$. Evaluating the power absorbed, we have

$$\begin{aligned} P_{abs} &= \frac{1}{2}\int_0^R \frac{J_\theta^2(r)}{\sigma_{eff}} 2\pi r l \, dr \\ &= \frac{1}{2} I_{rf}^2 \frac{\pi e^2 n_0 \nu_{eff} \mu_0^2 \mathcal{N}^2 R^4}{8ml} \end{aligned} \tag{12.2.3}$$

such that

$$P_{abs} \propto n_0 I_{rf}^2 \tag{12.2.4}$$

In this low-density regime where the fields fully penetrate the plasma, the power absorbed is simply proportional to the number (density) of electrons in the discharge. Comparing (12.2.1) with (12.2.4) and holding $I_{rf}$ fixed, we see that $P_{abs}$

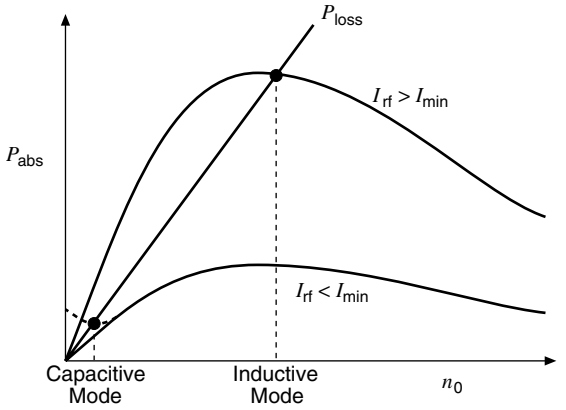


**Figure 12.4.** Absorbed power versus density from the inductive source characteristics (curves) for two different values of the driving current $I_{rf}$, and power lost versus density (straight line); the dotted curve includes the additional capacitive power at low density for $I_{rf} < I_{min}$.

versus $n_0$ has a maximum near $\delta_p \sim R$. This corresponds to a variation with density as sketched as the solid curves in Figure 12.4 for two different values of $I_{rf}$. Now consider the power balance requirement (10.2.14), which is plotted as a straight line in the figure. The intersection of this line with each of the solid curves defines the equilibrium point for inductive discharge operation for that particular value of $I_{rf}$. The intersection shown at $I_{rf} > I_{min}$ gives an inductive mode equilibrium. We see that inductive source operation is impossible if the source current $I_{rf}$ lies below some minimum value $I_{min}$. However, a weak capacitive discharge can exist for $I_{rf} < I_{min}$, as we describe in the following subsection.

### Capacitive Coupling

At this point the reader might ask: since a high voltage $V_{rf} \approx 1870$ V exists at the high-voltage end of the coil, what is the effect of capacitive coupling on the discharge? We will see below that for high densities only a small fraction of $V_{rf}$ appears across the sheath, such that the additional ion (and electron) energy loss is small. However, at low densities, the capacitive coupling can be the major source of power deposition.

To estimate the rf voltage across the sheath, $\tilde{V}_{sh}$, at the high-voltage end of the coil, we note that the sheath capacitance per unit area is $\sim \epsilon_0/s_m$ and the capacitance per unit area of the dielectric cylinder is $\sim \epsilon_0/(b - R)$. Assuming that the plasma is at ground potential, then the voltage across the sheath is found from the capacitive voltage divider formula,

$$\tilde{V}_{sh} = V_{rf} \frac{s_m}{b - R + s_m} \tag{12.2.5}$$

Using the modified Child law (11.2.15), we calculate the sheath thickness from

$$en_s u_B = 0.82\,\epsilon_0 \left(\frac{2e}{M}\right)^{1/2} V_{rf}^{3/2} \left(\frac{s_m}{b - R + s_m}\right)^{3/2} \frac{1}{s_m^2} \tag{12.2.6}$$

which is a cubic equation in $s_m$. However, for high densities for which $s_m \ll b - R$, (12.2.6) simplifies to

$$s_m \approx \left(\frac{0.82\,\epsilon_0}{en_s u_B}\right)^2 \left(\frac{2e}{M}\right) \frac{V_{rf}^3}{(b - R)^3} \tag{12.2.7}$$

The RHS is generally small for the usual voltages of inductive discharges, so that $s_m$ is much smaller than in a capacitive discharge. In our example, we find $s_m \approx 6.4 \times 10^{-4}$ cm, so that, from (12.2.5), $\tilde{V}_{sh} \approx 0.22$ V. Actually, for a sheath this thin, the high-voltage sheath relation (12.2.6) is not valid. From (2.4.23), the Debye length is $\lambda_{De} \approx 3.8 \times 10^{-3}$ cm. The sheath is a few Debye lengths thick. Using calculations for capacitive discharges (see Godyak and Sternberg, 1990b), we estimate $s_m \sim 2 \times 10^{-2}$ cm, such that (12.2.5) yields $\tilde{V}_{sh} \sim 9$ V, which contributes only a small correction to the dc sheath voltage.

From the relations (12.1.20)–(12.1.23), we can see one reason why the designer wants to keep the number of turns of the exciting coil small in a high density discharge. From (12.1.20) and (12.1.21), we see that $Z_s \propto \mathcal{N}^2$, and at fixed $P_{abs}$, from (12.1.22), we find $\tilde{I}_{rf} \propto 1/\mathcal{N}$. Then (12.1.23) gives $\tilde{V}_{rf} \propto \mathcal{N}$. From (12.2.7), we see that $s_m \propto \mathcal{N}^3$ at a fixed density, such that doubling $\mathcal{N}$ would increase $s_m$ by almost an order of magnitude. The increased ion energy loss across this larger sheath (increased $\mathcal{E}_T$) leads to lower density and generally less favorable discharge parameters.

In contrast to the high-density case, at low densities the sheath width $s_m$ becomes comparable to or larger than the vacuum (or dielectric) window gap width $b - R$, and from (12.2.6) most of $V_{rf}$ can be dropped across the sheath. From (11.2.33) or (11.2.34), the capacitive power increases with increasing $\tilde{V}_{sh}$, and from (12.2.5), $\tilde{V}_{sh}$ increases with decreasing density $n_0$ (increasing sheath thickness $s_m$). Therefore, the capacitive power absorbed increases with decreasing $n_0$. In this regime, any discharge must be capacitively driven. Including the additional capacitively coupled power due to the sheath voltage (12.1.24) gives the dotted curve in Figure 12.4 at low densities instead of the solid curve for $I_{rf} < I_{min}$. There is an intersection with the $P_{loss}$ line and, therefore, a capacitive mode equilibrium at low densities. Increasing $I_{rf}$ from below $I_{min}$, this low-density capacitive plasma makes a relatively abrupt transition to a high density inductive mode when $I_{rf}$ exceeds $I_{min}$. Decreasing $I_{rf}$ in inductive mode results in a similar inductive-to-capacitive transition when $I_{rf}$ falls below $I_{min}$. The capacitive coupling is very convenient for start-up of an inductive discharge, as the ignition relies on a high voltage in the discharge chamber, before the high-density inductive plasma is formed.

### Hysteresis and Instabilities

Various additional plasma and circuit effects can produce a *hysteresis* in the discharge characteristics, in which the capacitive-to-inductive transition occurs at a higher rf coil current $I_{min2}$ than the inductive-to-capacitive transition at $I_{min1}$. For the range of currents between $I_{min1}$ and $I_{min2}$, the mode actually present depends on the history of the system. Hysteresis of discharge characteristics is often seen experimentally, and an explanation in terms of power balance arguments has been given by Turner and Lieberman (1999). For example, considering again the power balance curves shown in Figure 12.4, with capacitive coupling present, it can be seen (Problem 12.5) that there is only a single intersection of the $P_{abs}$ and $P_{loss}$ curves as the current is varied, yielding a discharge characteristic without hysteresis. However, if the $P_{loss}$ versus $n_e$ curve is not linear but has a convex curvature, or if the curve is linear but is displaced upward from the origin ($P_{loss} > 0$ for $n_e = 0$), then there is a range of currents where there are three intersections, such that the discharge characteristic has hysteresis. The low-density intersection in a stable capacitive equilibrium, the high-density intersection is a stable inductive equilibrium, and the intermediate density intersection is an unstable equilibrium. Mechanisms that can produce a convex curvature (nonlinearity) for the $P_{loss}$ curve include multistep ionization, electron distribution function changes due to electron–electron collisions, and a reduction in inductive coupling due to a capacitive rf sheath (Turner and Lieberman, 1999).

A modified $P_{loss}$ curve can also be produced by the presence of negative ions in the discharge. In this latter case, the additional dynamics of negative ion generation and destruction can result in an instability, in which there is no stable discharge equilibrium. Experimentally, it is found that if the plasma contains negative ions; for example, from feedstock gases such as $O_2$, $SF_6$, $Cl_2$, and $CF_4$, that over a significant power range around the transition between lower power capacitive operation and higher power inductive operation, there is a relaxation oscillation between high and low density modes. For example, an experiment to investigate these instabilities was performed in an $Ar/SF_6$ (1:1) gas mixture in a device 30 cm in diameter and 19 cm long, with a three-turn planar coil driven at 13.56 MHz (see Section 12.3). At a pressure of 5 mTorr, with an average absorbed power of 550 W, the relaxation oscillation shown in Figure 12.5 was found (Chabert et al., 2001). Varying the power at this pressure, a range of oscillatory (unstable) behavior was found between $P_{abs} = 400$ W and $P_{abs} = 700$ W. Above 700 W the plasma was stable in the inductive mode with ion and electron densities in the higher density range, and below 400 W the ion and electron densities were more than a factor of 10 lower, characteristic of capacitively driven operation.

To analyze the process, the three time-varying equations of an electronegative plasma for positive ion, negative ion, and electron energy balance were solved, using a global model (see Chapter 10), together with the conditions of quasi-neutrality and Boltzmann electrons. However, we can understand the instability mechanism in a rather straightforward way from the electron energy balance

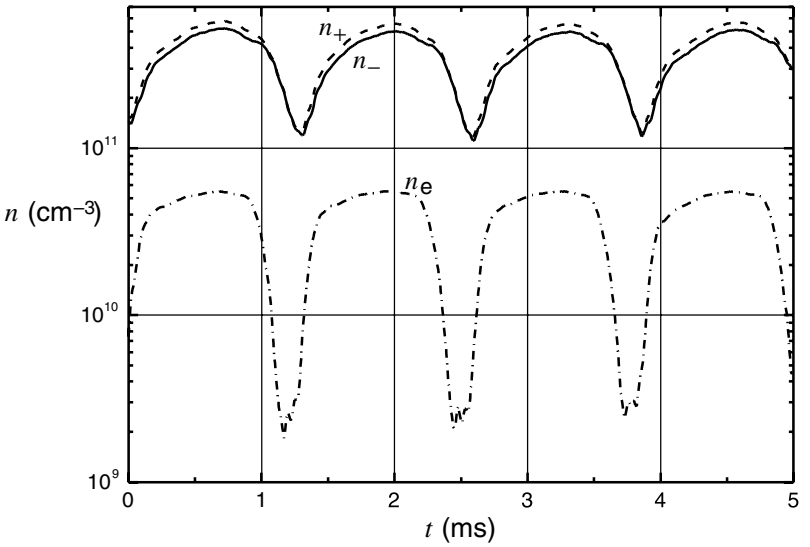


**Figure 12.5.** Positive ion, negative ion and electron densities as a function of time for 1:1 $Ar/SF_6$ mixture; the total pressure is 5 mTorr, the average power absorbed is 550 W.

alone. As for pulsed power discharges in (10.6.5), we have

$$\mathcal{V}\frac{\mathrm{d}}{\mathrm{d}t}\left(\frac{3}{2}en_\mathrm{e}\mathrm{T_e}\right) = P_\mathrm{abs} - P_\mathrm{loss} \tag{12.2.8}$$

For the losses, in keeping with a global approximation, we use the volume and surface losses, and consider $\alpha_0 = n_-/n_\mathrm{e} \gg 1$, such that $n_- \approx n_+$, to obtain

$$P_\mathrm{loss} = K_\mathrm{iz}e\mathcal{E}_\mathrm{c}dAn_\mathrm{g}n_\mathrm{e} + h_l u_{\mathrm{B}\alpha}e(4.8\mathrm{T_e} + 2\mathrm{T_e})An_- \tag{12.2.9}$$

where $h_l$ is an edge-to-center density ratio for an electronegative plasma and $u_{\mathrm{B}\alpha} = (e\mathrm{T}_-/\mathrm{M})^{1/2}$.

For the absorbed power (solid curve in Fig. 12.4) we take a sum of inductive and capacitive powers

$$P_\mathrm{abs} = \frac{1}{2}I_\mathrm{rf}^2 R_\mathrm{abs}\left(\frac{n_\mathrm{ind}n_\mathrm{e}}{n_\mathrm{ind}^2 + n_\mathrm{e}^2} + \frac{n_\mathrm{cap}}{n_\mathrm{cap} + n_\mathrm{e}}\right) \tag{12.2.10}$$

where the first and second terms approximate the inductive and capacitive powers, with parameters $R_\mathrm{abs}$ a resistance chosen to give the correct power, at the power maximum, $n_\mathrm{ind}$ chosen to give the correct maximum of the inductive power versus $n_\mathrm{e}$, as in Figure 12.4, and $n_\mathrm{cap}$ chosen to give the correct ratio of capacitive-to-inductive power at some low density, falling off with $n_\mathrm{e}$ at higher densities.

With the further observation that the electron density can build up and decay much more rapidly than the negative ion density, particularly for high $\alpha_0$, we obtain the physical instability mechanism illustrated in Figure 12.6. From (12.2.9), with $T_e$ nearly constant, the power loss has the form $P_{loss} = K_e n_e + K_- n_-$, with constants $K_e$ and $K_-$. This gives a linear variation of $P_{loss}$ with $n_e$ whose intercept at $n_e = 0$ is proportional to the slowly varying negative ion density $n_-$. The two loss curves, $P_{loss1}$ and $P_{loss3}$, have been chosen at the two tangencies with the $P_{abs}$ curve. At the end of phase 4, the loss curve decreases below the $P_{loss1}$ curve, the quasi-capacitive equilibrium is lost, and the discharge enters phase 1, with $n_e$ increasing rapidly due to ionization. Similarly, at the end of phase 2, during which the negative ion density builds up, the loss curve increases above $P_{loss3}$. The quasi-inductive equilibrium is lost, and the discharge enters phase 3, with the loss of positive ions in the escaping flux being matched by a rapid loss of the lower density electrons, The decay of the negative ions toward a lower density equilibrium, in phase 4, then repeats the relaxation oscillation cycle.

The rapid rise and fall of the electron density, seen in Figure 12.5, are consistent with this physical mechanism. The time scale of the relaxation oscillation is set by the build-up and decay of the negative ions, with the scaling determined from

$$\frac{1}{n_-}\left(\frac{dn_-}{dt}\right)_{decay} \approx K_{rec} n_- \approx (K_{att} K_{rec} n_g n_e)^{1/2} \tag{12.2.11}$$

where the second equality follows by use of (10.4.24). The $n_g$ and $n_e$ scalings have been qualitatively seen experimentally.

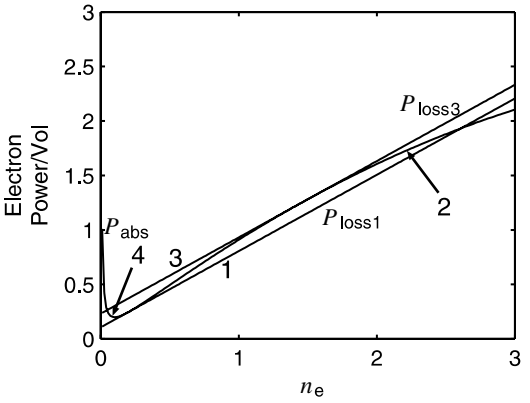


**Figure 12.6.** Absorbed electron power $P_{abs}$ versus electron density $n_e$ and two different curves of electron power lost versus $n_e$ ($P_{loss1}$ at a low negative ion density $n_-$ and $P_{loss3}$ at a high $n_-$).

## Power Transfer Efficiency

Let us note that the driving coil (primary of the transformer shown in Fig. 12.2) has some resistance $R_{\text{coil}}$. Hence, even if the discharge is extinguished ($n_0 = 0$), there is a minimum power $P_{\text{Tmin}} = \frac{1}{2} I_{\text{min}}^2 R_{\text{coil}}$ supplied by the source. Because $P_{\text{abs}} \propto n_0^{-1/2}$ at high densities, we see from Fig. 12.4 that the power transfer efficiency $P_{\text{abs}}/P_{\text{T}}$ falls continually as $n_0$ is increased, hence limiting source operation at high densities because of power supply limitations. Although $\delta_{\text{p}} \sim R$ is the preferred operating regime for maximum power efficiency, other considerations often indicate operation at lower or higher densities. The poor power transfer to the plasma at very low and at very high densities is analogous to the well-known property of an ordinary transformer with an open and a shorted secondary winding. In both cases no power is dissipated in the load (here the plasma), but in both cases there is power dissipated in the primary winding (here the coil) due to its inherent resistance. Piejak et al. (1992) have given a complete analysis of an inductive discharge in terms of measurable source voltages and currents, based on this analogy.

For completeness, we note that at very high densities, the electron–ion collision frequency may be larger than the electron–neutral collision frequency. In this collisional regime, $\nu_{90}$ from (3.3.7) replaces $\nu_{\text{m}}$ in determining $\sigma_{\text{dc}}$. Since $\nu_{90} \propto n_0$ (the Spitzer conductivity is independent of $n_0$), the scaling (12.2.1) is replaced by

$$P_{\text{abs}} \propto I_{\text{rf}}^2$$

independent of $n_0$ in this regime. However, low-pressure inductive discharges for materials processing are rarely operated at such high densities.

## Exact Solutions

One-dimensional solutions over the entire range of densities can be given for the case where a uniform density plasma fills a long cylindrical coil ($b = R$ and $l \gg R$). These were first obtained by Thomson (1927) in the collisional (high pressure) regime $\nu_{\text{m}} \gg \omega$, where the penetration of the rf fields into the discharge is governed by the collisional skin depth (12.1.6). Here we extend Thomson's treatment to the entire range of collisionalities from $\nu_{\text{m}} \ll \omega$ to $\nu_{\text{m}} \gg \omega$. Maxwell's equations (2.2.1) and (2.2.2) for the $\tilde{E}_\theta$ and $\tilde{H}_z$ field components are

$$\frac{\text{d}}{\text{d}r}(r\tilde{E}_\theta) = -j\omega\mu_0 r\tilde{H}_z \tag{12.2.12}$$

$$-r\frac{\text{d}\tilde{H}_z}{\text{d}r} = j\omega\epsilon_0\kappa_{\text{p}}(r\tilde{E}_\theta) \tag{12.2.13}$$

with $\kappa_{\text{p}}$ given by (12.1.2). Eliminating $r\tilde{E}_\theta$ from these equations, we obtain

$$\frac{\text{d}^2\tilde{H}_z}{\text{d}r^2} + \frac{1}{r}\frac{\text{d}\tilde{H}_z}{\text{d}r} + k_0^2\kappa_{\text{p}}\tilde{H}_z = 0 \tag{12.2.14}$$

which is Bessel's equation with $k_0 = \omega/c$. With the boundary condition that $\tilde{H}_z(R) = H_{z0}$, the solution is

$$\tilde{H}_z = H_{z0}\frac{\mathrm{J}_0(kr)}{\mathrm{J}_0(kR)} \tag{12.2.15}$$

where

$$k = k_0\sqrt{\kappa_\mathrm{p}} \tag{12.2.16}$$

is the complex propagation constant. We see that the Bessel functions have complex argument. Using (12.2.15) to evaluate the LHS of (12.2.13), and solving for $\tilde{E}_\theta$, we obtain

$$\tilde{E}_\theta = H_{z0}\frac{k}{j\omega\epsilon_0\kappa_\mathrm{p}}\frac{\mathrm{J}_1(kr)}{\mathrm{J}_0(kR)} \tag{12.2.17}$$

The time-average power flowing into the discharge is found in terms of the field amplitudes at the plasma surface $r = R$ using the complex Poynting theorem (Ramo et al., 1984),

$$P_\mathrm{abs} = 2\pi RlS_\mathrm{abs} = 2\pi Rl\,\mathrm{Re}\left(-\frac{1}{2}\tilde{E}_{\theta 0}H_{z0}\right) \tag{12.2.18}$$

As the plasma density $n$ is increased from zero at fixed $\omega$, $R$, and $H_{z0}$ (equivalent to holding the coil current fixed), then one finds from (12.2.18) that $P_\mathrm{abs}$ rises from zero to a maximum and then falls to zero. The variation is similar to that shown in the solid curves of Figure 12.4. For a nearly collisionless plasma $\nu_\mathrm{m} \ll \omega$, one finds a maximum power at a density such that $\delta_\mathrm{p} \approx 0.37\,R$. For a collisional plasma $\nu_\mathrm{m} \gg \omega$, one finds a maximum power at $\delta_\mathrm{c} \approx 0.57\,R$. Hence in both cases the maximum power efficiency (for a coil having a finite resistance) occurs when the appropriate skin depth is of order of the plasma radius.

Other issues of inductive discharge operation include finite geometry effects ($l \sim R$), planar coil source operation, startup, and self-resonant coil effects due to stray coil capacitances. We address some of these issues in the following sections, and refer the reader to the literature (Piejak et al., 1992; Eckert, 1986; Hopwood et al., 1993a,b) for further information.

## 12.3 PLANAR COIL CONFIGURATION

The planar coil discharge shown in Figure 12.1*b*, with or without multipole magnets, is a commonly used configuration for materials processing, typically generating relatively uniform low aspect ratio plasmas with densities between $10^{11}$ and $10^{12}$ cm$^{-3}$

over substrate diameters of 20 cm or more. In axisymmetric geometry, the coil generates an inductive field having magnetic components $\tilde{H}_r(r,z)$ and $\tilde{H}_z(r,z)$, and an electric component $\tilde{E}_\theta(r,z)$. As shown in Figure 12.7*a*, the rf magnetic field lines in the absence of a plasma encircle the coil and are symmetric with respect to the plane of the coil. If a plasma is formed below the coil, as shown in Figure 12.7*b*, then from Faraday's law (2.2.1), an azimuthal electric field $\tilde{E}_\theta$ and an associated current density $\tilde{J}_\theta$ are induced within the plasma. The plasma current, opposite in direction to the coil current, is confined to a layer near the surface having a thickness of order the skin depth $\delta$. The total magnetic field, which is the sum of the fields due to the $\mathcal{N}$ turn exciting coil current and the "single-turn" induced plasma current, is shown in Figure 12.7*b*. The dominant magnetic field components within the plasma are $\tilde{H}_z$ near the axis and $\tilde{H}_r$ away from the axis, as shown. Near the axis, Faraday's law implies that both $\tilde{E}_\theta$ and $\tilde{J}_\theta$ vanish as $\tilde{E}_\theta, \tilde{J}_\theta \propto r$. This implies that the absorbed power density,

$$p_{\text{abs}} = \tfrac{1}{2}\text{Re}\,\tilde{J}_\theta \tilde{E}_\theta^* \tag{12.3.1}$$

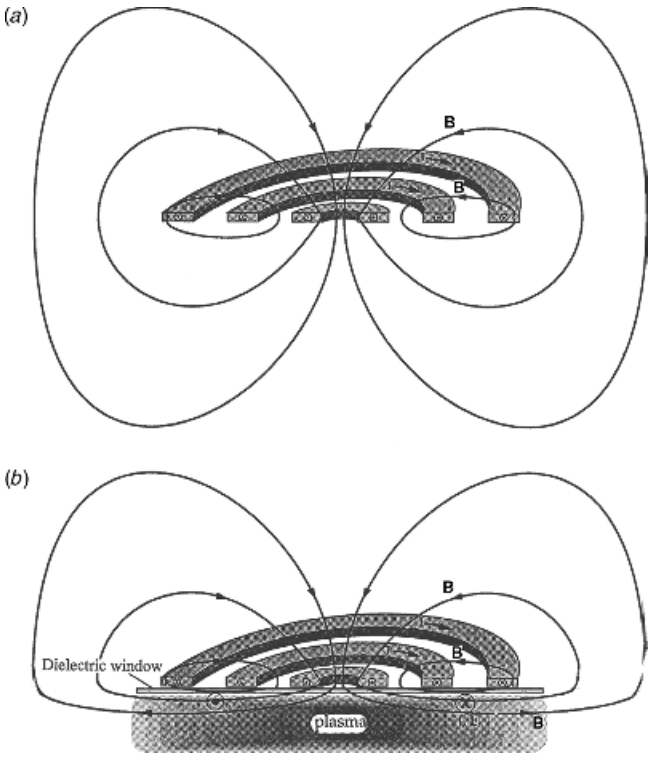


**Figure 12.7.** Schematic of the rf magnetic field lines near a planar inductive coil (*a*) without nearby plasma and (*b*) with nearby plasma (after Wendt, 1993).

vanishes on axis, leading to a ring shaped profile for the absorbed power. The transformer model of the previous section can be applied to the planar configuration, but the inductance matrix elements are difficult to determine from simple electromagnetic models (Gudmundsson and Lieberman, 1998).

The rf magnetic fields within the plasma have been measured by Hopwood et al. (1993a) for an inductive discharge excited by a planar square coil, which was separated from a rectangular aluminum plasma chamber 27 cm on a side and 13 cm high by a 2.54-cm thick quartz window. Although this system is not axisymmetric, the general structure of the fields and the absorbed power profile are similar to those in an axisymmetric system. We use Hopwood's results to illustrate the general features observed in planar inductive discharges.

Figure 12.8 shows the measured variation of $B_r \equiv |\tilde{B}_r|$ with $z$ at $r = 6.3$ cm in a 5-mTorr oxygen discharge. The field decreases exponentially with distance from the window, with a maximum of 2.7–5.1 G, depending on the incident power $P_{\rm inc}$, and with a skin depth $\delta$ (characteristic length for the exponential decay) varying from 2.1 to 2.7 cm, and scaling roughly as $P_{\rm inc}^{-1/2}$, in agreement with (12.1.4) or (12.1.6) with $n_0 \propto P_{\rm inc}$. In general, the skin depth lies between the values $\delta_{\rm p}$ and $\delta_{\rm c}$ given by (12.1.4) and (12.1.6), and is fairly close to both. Figure 12.9 shows the measured variation of $B_r$ with $r$ (along the diagonal of the chamber) at three different positions below the window in a 5-mTorr, 500-W, argon discharge. We see that $B_r$ falls to zero on the axis and has a maximum at approximately 9.5 cm off the axis.

The rf electric field $\tilde{E}_\theta$ can be related to $\tilde{B}_r \equiv \mu_0 \tilde{H}_r$ by using the $r$ component of Faraday's law (2.2.1),

$$\frac{\partial \tilde{E}_\theta}{\partial z} = j\omega\mu_0 \tilde{H}_r \tag{12.3.2}$$

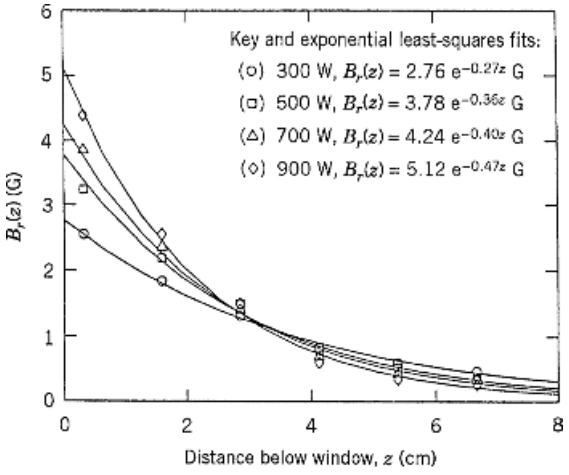


**Figure 12.8.** Radio frequency magnetic induction amplitude $|\tilde{B}_r|$ versus $z$ in a 5-mTorr oxygen discharge. The solid lines are a least-squares fit to the data (Hopwood et al., 1993a).

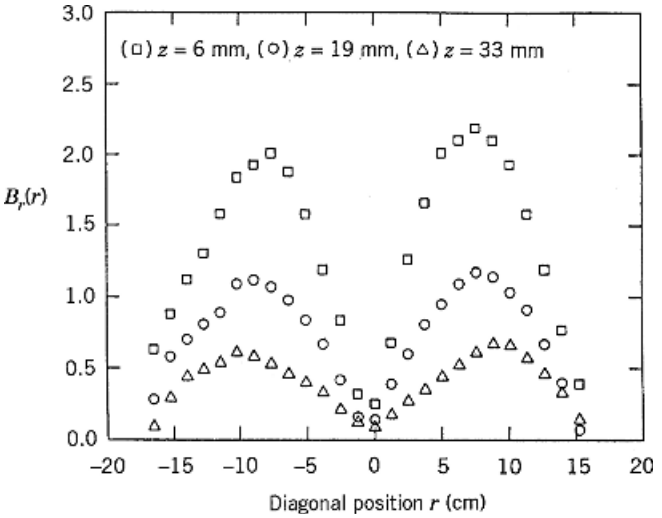


**Figure 12.9.** Radio frequency magnetic induction amplitude $|\tilde{B}_r|$ versus diagonal radius $r$ at three different distances below the window as measured in a 5-mTorr, 500-W argon discharge (Hopwood et al., 1993a).

Assuming that $\tilde{E}_\theta = \tilde{E}_{\theta 0}\, e^{-z/\delta}$ and inserting this into (12.3.2), we obtain

$$\tilde{E}_\theta = -j\omega\mu_0 \delta \tilde{H}_r \tag{12.3.3}$$

Hence $\tilde{E}_\theta$ has the same axial and radial variation as $\tilde{B}_r$ given in Figures 12.8 and 12.9.

In addition to the field measurements, Langmuir probes (see Section 6.6) were used to determine the ion density $n_i$, electron temperature $T_e$, and plasma potential $V_s$ (Hopwood et al., 1993b). The ion density measurement was confirmed by comparison to a 35-GHz microwave interferometer measurement (see Section 4.6). Figure 12.10 shows $n_i$ versus incident power $P_{inc}$ at a location on-axis and 5.7 cm ($\sim$3 skin depths) below the window, for pressures between 0.5 and 15 mTorr in argon. We see that $n_i$ varies linearly with $P_{inc}$, but that $n_i \approx 0$ (on a $10^{11}$-cm$^{-3}$ scale) at approximately 100 W. Below this incident power, an inductive discharge cannot be sustained (see Section 12.2), and a low-density plasma is sustained by capacitive coupling between the coil and the plasma.

Figure 12.11 shows the measured variation of $n_i$,$T_e$, and $V_s$ with argon pressure for $P_{inc} = 500$ W. We see that $T_e$ falls slowly as $p$ increases, as determined from an ion particle balance relation; for example, (10.2.12) plotted in Fig. 10.1. The ion density is seen to increase with increasing pressure. This is consistent with the power balance relation, which indicates that the density varies inversely with the effective plasma area, as follows. For this discharge, with $l = 13$ cm and $R \gg l$,

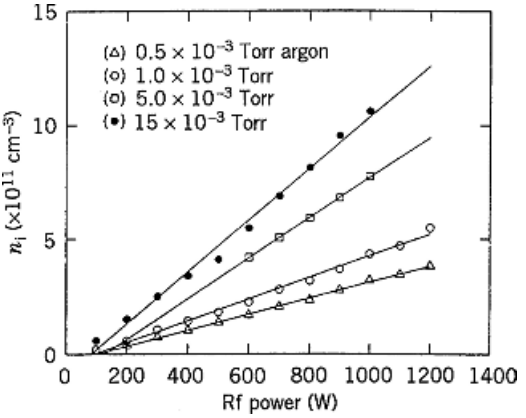


**Figure 12.10.** Ion density versus rf power and argon pressure (Hopwood et al., 1993b).

we can estimate that $A_{\text{eff}}$ in (10.2.11) scales as

$$A_{\text{eff}} \propto h_l \propto \left(3 + \frac{l}{2\lambda_{\text{i}}}\right)^{-1/2} \tag{12.3.4}$$

Using (3.5.7) to determine the ion–neutral mean free path $\lambda_{\text{i}}$ in argon, we find $\lambda_i \approx 3$ cm at 1 mTorr and $\lambda_i \approx 0.15$ cm at 20 mTorr. Hence from (10.2.15), the

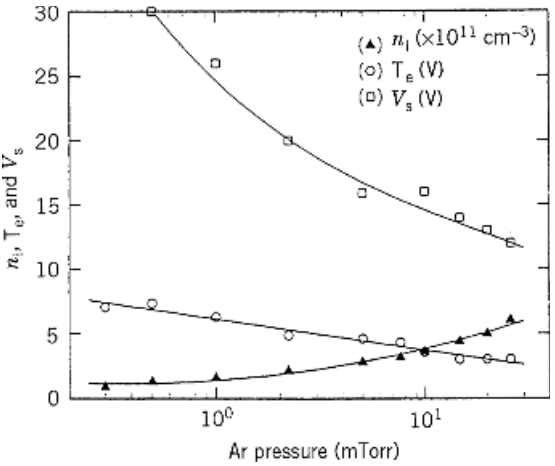


**Figure 12.11.** Ion density, electron temperature, and plasma potential versus argon pressure in a 500-W discharge with magnetic multipole confinement (Hopwood et al., 1993b).

predicted density ratio is

$$\frac{n_i(20\text{ mTorr})}{n_i(1\text{ mTorr})} \approx \frac{A_{\text{eff}}(1\text{ mTorr})}{A_{\text{eff}}(20\text{ mTorr})} \approx \frac{0.44}{0.15} \approx 3.0$$

which is in reasonable agreement with the measured ratio of ~3.3 obtained from Figure 12.11. The plasma potential $V_s$ is seen to lie between 12 and 30 V, roughly consistent with (10.2.4). The potential increases as the pressure decreases, in qualitative agreement with the scaling predicted from (10.2.4).

All preceding measurements were performed with multipole magnets placed along the four 27-cm × 13-cm sidewall areas (see Section 5.4). In Figure 12.12, the normalized ion saturation current (proportional to the density) is plotted along a diagonal within the chamber with and without the multipole magnets in place, for a 5-mTorr oxygen discharge. We see that the multipole magnets greatly increase the uniformity of the density. The ratio of the standard deviation to the average density across the central 20 cm of the discharge with multipole magnets was measured to be 2.5 percent. This result is qualitatively consistent with the dominant losses being axial, when quadrupoles are present.

A relatively complete set of characterization measurements of a planar inductive argon discharge has been given by Godyak and collaborators (Godyak et al., 1994, 1999, 2002; Godyak and Piejak, 1997). External electrical characteristics such as voltage, current phase angle, resistance, reactance, and coupling efficiency were measured over a wide range of discharge powers, driving frequencies, and gas pressures. Magnetic probes were used to determine the internal rf electric and magnetic fields and currents, and Langmuir probes were used to determine the electron energy distribution function and plasma parameters such as density, average energy, and effective collision frequency. The transition from collisional to stochastic heating was observed as the pressure was lowered. In the stochastic (nonlocal) regime,

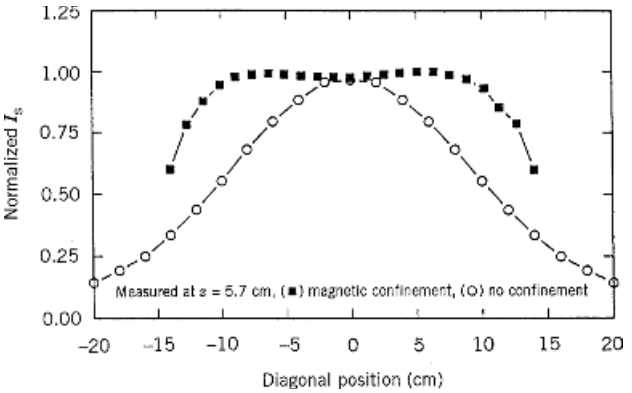


**Figure 12.12.** Normalized ion saturation current measured across the diagonal of the plasma chamber with and without magnetic multipole confinement (Hopwood et al., 1993b).

the expected nonexponential decays of the field profiles were observed. At low frequencies, strong nonlinear effects were measured, including second-harmonic currents and ponderomotive forces.

## 12.4 HELICAL RESONATOR DISCHARGES

Helices have long been used to propagate electromagnetic waves with phase velocity $v_{ph} \ll c$, the velocity of light. This property allows a helix to resonate in the MHz range such that it can be used for efficient plasma generation at low pressures. Low-pressure operation makes it particularly useful for etching, and it has also been useful for deposition of silicon dioxide and silicon nitride films (Cook et al., 1990). Helical resonator plasmas operate conveniently at radio frequencies (3–30 MHz) with simple hardware, do not require a dc magnetic field (as do ECRs and helicons; see Chapter 13), exhibit high $\mathcal{Q}$ (600–1500 typically without the plasma present), high characteristic impedance ($Z_0$), and can be operated without a matching network. As shown in Figure 12.13, the source consists of a coil surrounded by a grounded coaxial cylinder. The composite structure becomes resonant when an integral number of quarter waves of the rf field fit between the two ends. When this condition is satisfied, the electromagnetic fields within the helix can sustain a plasma with low matching loss at low gas pressure.

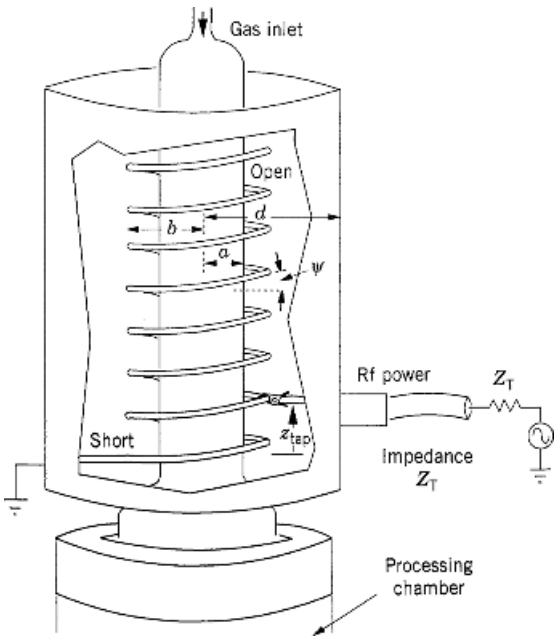


**Figure 12.13.** Schematic of a helical resonator plasma source.

We have seen for inductive discharges at low density that the ohmic heating is not sufficient to sustain the discharge, which then operates similarly to a capacitive discharge at much lower density and higher sheath voltage (larger sheaths). We expect the same general behavior to occur in the resonant helical discharge, because of the voltage divider action between the rf voltage across the sheath and that which appears across the fixed spacing between the helix and the vacuum chamber. Because the helix is a resonant device, large voltages necessarily appear somewhere between the helix and the plasma, such that it is more difficult to operate in a purely inductive regime. To force operation in this regime, an electrostatic shield can be added between the helix and the plasma column to reduce the capacitive coupling to a negligible value. The shield is typically a metal cylinder slotted along $z$ that allows the inductive field $\tilde{E}_\theta$ to penetrate into the plasma, while shorting out the capacitive $\tilde{E}_r$ and $\tilde{E}_z$ fields. Using this configuration, discharges as large as 25 cm in diameter have been produced experimentally, driven by up to 5 kW of rf power at 13.56 MHz and producing plasmas with densities (in argon) exceeding $2 \times 10^{12}\ \mathrm{cm}^{-3}$.

An analysis, with comparison to experiments, has been performed on an unshielded helical discharge at lower powers, where both stochastic heating and ohmic heating are important (Niazi et al., 1994). We describe some features of this discharge here. Some, but not all, of the results are relevant to shielded discharges at higher powers. The basic design parameters for a helical resonator discharge consist of pressure, rf power, source length, plasma radius, helix radius, outer cylinder radius, winding pitch angle, and excitation frequency. For an unshielded plasma column, the wave dispersion, $k_z$ versus $\omega$, and the relation among the field quantities, have been determined in the approximation of a uniform, collisionless ($\omega \gg \nu_m$) plasma having relative dielectric constant $\kappa_p = 1 - \omega_{pe}^2/\omega^2$ [see (4.2.24)] by using a *sheath helix model*, in which the rf current in the helical wires is replaced by a continuous current sheet ("sheath") (Niazi et al., 1995). With an outer conductor, there are generally two modes, a helix mode, whose axial wavenumber is associated with the helix pitch angle $\Psi$,

$$k_{zh} \approx \frac{\omega}{c \tan \Psi} \tag{12.4.1}$$

and a coax mode, associated with a transverse electromagnetic wave propagating near the speed of light, $k_{z0} \approx \omega/c$. The useful mode is the helix mode. The mode has a resonance $k_z \to \infty$ at relatively low density, such that $\omega_{pe} = \omega$, and exists above that density. At large density, the plasma and outer cylinder are at nearly the same voltage, and the helix is at a high voltage with respect to them both. In this high-density limit the plasma acts like a conducting cylinder. During typical source operation, only the helix mode is resonant, and it dominates the source operation. A simple estimate of the resonant frequency from (12.4.1) gives $f \approx 25$ MHz at $l = 30$ cm ($k_z = 5.2\ \mathrm{m}^{-1}$). Greater accuracy can be obtained by analyzing the helix–plasma configuration in cylindrical geometry. End effects can change the resonant frequency due to additional capacitive coupling.

Once the resonant frequency for quarter wavelength operation is determined, then the fields within all regions inside the helical resonator can be found. From the fields in the plasma, the absorbed power can be found. This has been done for a quasistatic field approximation in the capacitively coupled regime where both ohmic and stochastic heating (see Sections 11.1 and 11.2) contribute to the power absorbed by the electrons. The calculation has not been performed for the inductive configuration (with an electrostatic shield), where only $\tilde{E}_\theta$ contributes to the absorbed power, but should be similar to that used for conventional inductive sources (see Section 12.1 and below).

For quarter-wavelength operation of a cylindrical sheath-current helix, the helix voltage $\tilde{V}_{\max}$ at the high-voltage end of the coil is determined in terms of the azimuthal component of sheath current per unit length $K_\theta$ at the low-voltage end of the coil to be

$$\tilde{V}_{\max} = \zeta\left(\frac{\mu_0}{\epsilon_0}\right)^{1/2} bK_\theta \tag{12.4.2}$$

where $\zeta$ is a geometric constant of order unity. For a helix with $\mathcal{N}$ turns the helix current $\tilde{I}_{\max}$ at the low-voltage end of the coil is obtained from $\mathcal{N}\tilde{I}_{\max} = lK_\theta$. Combining this with (12.4.2), we obtain the helix impedance

$$Z_0 = \frac{\tilde{V}_{\max}}{\tilde{I}_{\max}} = \zeta\left(\frac{\mu_0}{\epsilon_0}\right)^{1/2}\frac{\mathcal{N}b}{l}. \tag{12.4.3}$$

For an example with $a = 3$ cm, $b = 5$ cm, $d = 10$ cm, $l = 30$ cm, and $\Psi = 0.1$ rad, where the parameters are defined in Figure 12.13, we find $\mathcal{N} = 48$. Using the computed value $\zeta = 0.33$ gives $Z_0 = 995\ \Omega$. For a constant $l$ and a constant pitch angle of the helix, $\mathcal{N}b/l$ remains essentially constant with varying helix diameter, and since $\zeta$ changes relatively slowly, the impedance $Z_0 \sim 1\ \text{k}\Omega$ over a range of aspect ratios. This high helix impedance allows matching to a $50\ \Omega$ transmission line near a shorted end of the helix.

From (12.4.3), we see that the impedance, and also the voltage $\tilde{V}_{\max}$, increases as the number of helix turns $\mathcal{N}$ increases. We also found that to be true for inductive discharges in Section 12.1. For the geometry considered here, with $\mathcal{N}$ large, the result is to also have large sheath fields and accompanying large ion energy losses. The discharge is then operating in a mainly capacitive regime. The geometry of the helical resonator can also be changed to have a larger diameter with fewer turns. The approximate resonance condition, $k_{z\text{h}}l = m\pi/4$, with $m$ an integer, can also be written, using (12.4.1) with $\tan\Psi = l/2\pi b\mathcal{N}$, as

$$2\pi b\mathcal{N} = m\frac{\lambda}{4} \tag{12.4.4}$$

where $\lambda$ is the free space wavelength. A much larger radius $b$ with only five turns has, in fact, been experimentally investigated as a prototype reactor. In this configuration, the main difference between a five-turn inductive discharge of the type considered in Section 12.1 and the five-turn helical resonator considered here is that the latter is resonant, thus allowing a simple coupling, described in the following paragraph. However, a variable frequency (expensive) power supply may be required to maintain the resonance condition. Hence helical resonators have usually been driven using a fixed frequency supply in conjunction with a matching network.

To determine the power coupled from an external generator to the resonator, and the condition for a match (maximum power transfer), we consider the system shown schematically in Figure 12.13. The rf generator and its transmission line have characteristic impedances $Z_T$, with one side of the transmission line connected to the helix at the tap position $z_{tap}$ and the other side connected to the outer shield. Since the helix characteristic impedance $Z_0$ given in (12.4.3) is typically large compared to $Z_T$, we expect a match to occur with the tap made near the shorted end of the helical resonator, where the voltage is small and the current is large. This is, in fact what is found from a transmission line calculation and also in the experiments (Niazi et al., 1995; Park and Kang, 1997b). The shorted end of the helix acts as part of the matching system, allowing a good match over a wide range of parameters, without a matching network, provided the operating frequency is varied only over a modest range.

The analysis described above can be improved. In addition to the stochastic heating at the sheath edge and ohmic heating in the bulk plasma, ohmic heating in the sheath region and ionization in the sheath can also be included. Including these effects, a comparison has been made between theory and experiment, for the device shown schematically in Figure 12.13, for argon and nitrogen at 2- and 20-mTorr pressures. The results for the density versus absorbed power in argon at 20 mTorr shown in Figure 12.14 indicate, approximately, a $n \propto P_{abs}^{1/2}$ scaling, which is found in capacitive discharges when stochastic heating is the primary heating and when most of the energy loss is due to ions accelerated through a high-potential sheath. The dashed curve includes the additional power required to account for sheath losses.

The helical resonator propagation and matching characteristics are conveniently obtained from a circuit model (Park and Kang, 1997b). By measuring the input impedance characteristics as the tap position is varied, they determined the propagation constant. By matching the input resistance of the experiment to the model results they also determined the power absorption in the plasma, and the slight decay of the propagating signal away from the source.

A somewhat different resonator configuration was used by Vinogradov et al. (1998). They made the helical resonator a full wavelength long, which they called the *lambda-resonator.* The resonator had shorted ends and the power was injected in what they called a phase-balanced mode or capacitively compensated mode. The basic idea is that the voltages on the two halves of the resonator are out of phase, such that the plasma remains near rf ground potential. This minimizes

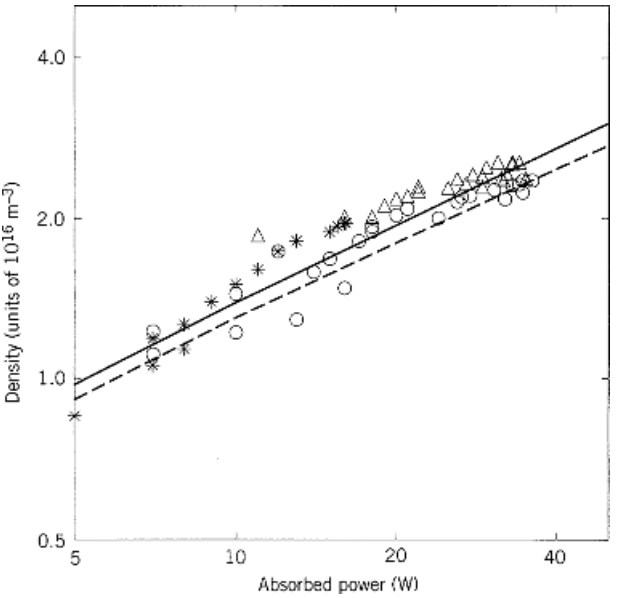


**Figure 12.14.** Measurements and model results for density versus absorbed power in a helical resonator. The symbols give the measured values for various runs; the solid and dashed lines give the analytic model results without and with the additional power required to account for sheath losses, respectively (Niazi et al., 1994).

capacitive current to the grounded surfaces, reducing various undesirable effects. They applied this concept to a relatively large practical device with an oxygen feedstock gas in the Torr pressure range, used for ashing (see Section 15.3). A typical high power operation with a 2 kW, 27.12 MHz matched source, produced a $n_e \approx 2 \times 10^{11}$ cm$^{-3}$ plasma inside a 235-mm diameter quartz chamber. Operation in the 10–50 mTorr range gave more intense heating in the regions of stronger helix current, indicating that the operation was primarily in the inductive mode at low pressures. The authors reported that the ashing rate exceeded that in conventional devices for a given power input due to the elimination of the dissipation associated with a conventional matching network.

## PROBLEMS

**12.1. Skin Depth** Consider a uniform electric field,

$$E_z(x,t) = \mathrm{Re}\,\tilde{E}_z(x)\,\mathrm{e}^{j\omega t}$$

at the surface of a half-space $x > 0$ of plasma having dielectric constant $\epsilon_p = \epsilon_0\kappa_p$ given by (12.1.2).

(a) Using Maxwell's equations (2.2.1) and (2.2.2) with $\mathbf{J}_T = \mathbf{J} + j\omega\epsilon_0\mathbf{E} = j\omega\epsilon_p\mathbf{E}$ and with $\mathbf{E} = \hat{z}E_z$ in the form given above, show that

$$\frac{d^2\tilde{E}_z}{dx^2} = -\frac{\omega^2}{c^2}\kappa_p\tilde{E}_z.$$

(b) Obtain the solution for $\tilde{E}_z(x)$ with the boundary conditions that $\tilde{E}_z = E_0$ at $x = 0$ and that $\tilde{E}_z$ is noninfinite as $x \to \infty$, and show that the electric field magnitude $|\tilde{E}_z(x)|$ decays exponentially into the plasma with a decay constant

$$\alpha = -\frac{\omega}{c}\,\mathrm{Im}\,\kappa_p^{1/2}$$

(c) Evaluate $\alpha$ in the two limits $\nu_m \ll \omega$ and $\nu_m \gg \omega$, thus verifying (12.1.3) and (12.1.5).

**12.2. Power Dissipation** Starting from the basic expression for power dissipation,

$$P_{abs} = \frac{1}{2}\int \mathbf{J}\cdot\mathbf{E}^*\,d\mathcal{V}$$

and with $|\mathbf{E}|$ decaying exponentially into the plasma with a decay constant $\alpha$ given by (12.1.3), with skin depth $\delta_p \ll R$, and with an effective collision frequency $\nu_{eff}$, obtain expression (12.1.10) for the absorbed power $P_{abs}$.

**12.3. Self- and Mutual Inductance of Concentric Solenoids** Consider two concentric solenoids of length $l$. The outer solenoid has $\mathcal{N}_1$ turns at radius $b$, and the inner solenoid has $\mathcal{N}_2$ turns at radius $R$. The elements of the inductance matrix are defined as

$$\Phi_1 = L_{11}I_1 + L_{12}I_2$$
$$\Phi_2 = L_{21}I_1 + L_{22}I_2$$

where $\Phi_i$ is the total magnetic flux linking the $\mathcal{N}_i$ turns of solenoid $i$ and $I_i$ is the feed current. The magnetic induction inside a solenoid having $\mathcal{N}_i$ turns each carrying a current $I_i$ is uniform and given by $B_{zi} = \mu_0\mathcal{N}_iI_i/l$. Using this and the above definition, for $\mathcal{N}_1 = \mathcal{N}$ and $\mathcal{N}_2 = 1$, obtain (12.1.14), (12.1.17), and (12.1.18) for the elements of the inductance matrix.

**12.4. Inductive Discharge Equilibrium**

(a) Verify all calculations for the example of inductive discharge equilibrium given in Section 12.1.

(b) Estimate the electron drift velocity $v_e$ within the skin depth layer, compare $\mathcal{E}_e = \frac{1}{2}mv_e^2/e$ to $T_e$, and comment on the validity of the global ionization model (10.2.12) for these discharge parameters.

**12.5. Hysteresis and Stability in an Inductive Discharge** Consider a low pressure, electropositive inductive discharge (no negative ions). The electron power absorption $P_{abs}$ is given by (12.2.10), which includes both inductive and capacitive power deposition.

(a) Assume a linear electron power loss $P_{loss} = K_e n_e$. Show that there is one and only one intersection of the $P_{abs}(n_e)$ and $P_{loss}(n_e)$ curves for any given value of $I_{rf}$. Hence show that there is no hysteresis in the capacitive-to-inductive transition.

(b) Consider now a nonlinear electron loss curve of the form $P_{loss} = K_e(n_e - an_e^2)$ with $an_e < 1$ over the density range of interest. Sketch the $P_{abs}(n_e)$ and $P_{loss}(n_e)$ curves for the cases of (i) one intersection and low $n_e$ (capacitive mode); (ii) one intersection and high $n_e$ (inductive mode); and (iii) three intersections (region of hysteresis).

(c) The stability of the intersections can be examined from the time-varying electron particle and energy conservation equations (10.6.1) and (12.2.8) as follows: Consider a small displacement $\Delta n_e > 0$ from the equilibrium value $n_{e0}$ at an intersection. If $P_{loss}(n_{e0} + \Delta n_e) > P_{abs}(n_{e0} + \Delta n_e)$, then from (12.2.8) we find that $T_e$ decreases. Hence $K_{iz}$ decreases and (10.6.1) shows that $n_e$ decreases; that is, $n_e$ will be restored to its equilibrium value $n_{e0}$. On the other hand, if $P_{loss}(n_{e0} + \Delta n_e) < P_{abs}(n_{e0} + \Delta n_e)$, then from (12.2.8) we find that $T_e$ increases. Hence $K_{iz}$ increases and (10.6.1) shows that $n_e$ increases, a runaway situation that yields an unstable equilibrium. Using this simple picture of stability of an equilibrium, investigate the stability of the intersections in (a) and (b).

**12.6. Discharge Equilibrium at High Pressure** For the same $R$, $b$, $l$, $\mathcal{N}$, $f$, $P_{abs}$, as in the example, but with a higher pressure $p = 50$ mTorr, find all the equilibrium discharge parameters.

**12.7. Discharge Equilibrium With Anomalous Skin Depth** For the same $R$, $b$, $l$, $\mathcal{N}$, $p$, and $P_{abs}$ as in the example, but with a lower frequency $f = 2$ MHz, find all the equilibrium discharge parameters. Assume that $\bar{v}_e/2\delta_e \gg \omega, \nu_m$.

**12.8. Discharge Equilibrium and Matching Network**

(a) Verify all calculations for the values of the matching network capacitors $C_1$ and $C_2$ given at the end of Section 12.1.

(b) Suppose $P_{abs}$ is increased from 600 to 1200 W in the example given in Section 12.1, with $R$, $b$, $l$, $\mathcal{N}$, $p$, and $f$ remaining the same. Find all the equilibrium discharge parameters.

(c) For part (b), determine values of $C_1$ and $C_2$ to match the discharge to a 50-$\Omega$ rf power source, using the procedure given at the end of Section 12.1.

**12.9. Minimum Current for an Inductive Discharge** For the same $R$, $b$, $l$, $\mathcal{N}$, $p$, and $f$ as given in the example of Section 12.1, use (12.2.3) to determine the minimum rf current amplitude $I_{min}$ to sustain an inductive discharge.